

Nearly free electrons in a 5d delafossite oxide metal

Pallavi Kushwaha,¹ Veronika Sunko,^{1,2} Philip J. W. Moll,³ Lewis Bawden,² Jonathon M. Riley,^{2,4} Nabhanila Nandi,¹ Helge Rosner,¹ Marcus P. Schmidt,¹ Frank Arnold,¹ Elena Hassinger,¹ Timur K. Kim,⁴ Moritz Hoesch,⁴ Andrew P. Mackenzie,^{1,2*} Phil D. C. King^{2*}

2015 © The Authors, some rights reserved; exclusive licensee American Association for the Advancement of Science. Distributed under a Creative Commons Attribution NonCommercial License 4.0 (CC BY-NC). 10.1126/sciadv.1500692

Understanding the role of electron correlations in strong spin-orbit transition-metal oxides is key to the realization of numerous exotic phases including spin-orbit–assisted Mott insulators, correlated topological solids, and prospective new high-temperature superconductors. To date, most attention has been focused on the 5d iridium-based oxides. We instead consider the Pt-based delafossite oxide PtCoO₂. Our transport measurements, performed on single-crystal samples etched to well-defined geometries using focused ion beam techniques, yield a room temperature resistivity of only 2.1 microhm-cm (μΩ-cm), establishing PtCoO₂ as the most conductive oxide known. From angle-resolved photoemission and density functional theory, we show that the underlying Fermi surface is a single cylinder of nearly hexagonal cross-section, with very weak dispersion along *k_z*. Despite being predominantly composed of *d*-orbital character, the conduction band is remarkably steep, with an average effective mass of only 1.14*m_e*. Moreover, the sharp spectral features observed in photoemission remain well defined with little additional broadening for more than 500 meV below *E_F*, pointing to suppressed electron-electron scattering. Together, our findings establish PtCoO₂ as a model nearly-free-electron system in a 5d delafossite transition-metal oxide.

INTRODUCTION

The delafossite structural series of oxides has recently attracted considerable attention because of the remarkable and varied properties of the compounds in the series. Its general formula is ABO₂, in which A is a noble metal (Pt, Pd, Ag, or Cu) and B is a transition metal (for example, Cr, Co, Fe, Al, and Ni) (1–4). The metal atoms are found in layers with triangular lattices, stacked along the perpendicular direction in various sequences, leading to structures similar to the layered rocksalt structure of the well-known ionic conductor LiCoO₂ and of NaCoO₂, which superconducts when intercalated by water. Interlayer coupling is weak, so the delafossites are quasi–two-dimensional.

The low temperature properties across the series vary considerably with A and B combinations. Known materials include candidate magnetoelectric insulators and thermoelectrics (5, 6), transparent conductors (7), and band insulators (1–4). There are also intriguing metals such as AgNiO₂ and PdCrO₂ in which the conduction takes place between Mott-insulating layers with magnetic order (8–13) and nonmagnetic metals with ultrahigh conductivity, such as PdCoO₂. Although they have been less studied than the layered perovskites, the delafossites have considerable potential for new physics and technology; epitaxial multilayers of delafossites and of delafossite/rocksalt combinations can be imagined. There is, therefore, a strong motivation to understand the fascinating properties of individual materials in the series.

In PdCoO₂, cobalt has formal valence of 3⁺ and the 3*d*⁶ configuration, meaning that the states at the Fermi level have dominantly Pd character (14–17), with a single half-filled band crossing the Fermi level. At 300 K, the resistivity (ρ) is 2.6 microhm-cm (μΩ-cm), lower per carrier than that of Cu (18). At low temperatures, both the shape and the

value of ρ are very unusual. It is best fitted by $\rho = \rho_0 + \beta e^{-T^*/T}$ (with β as a constant and *T*^{*} = 165 K) rather than the power law expected for standard phonon scattering. At least as surprising as the form of ρ is its value. A residual resistivity of only 7 nanohm-cm (nΩ-cm) has been reported (18). This corresponds to a mean free path (*ℓ*) of 20 μm, or ~1 × 10⁵ lattice spacings, an astonishing value in crystals grown from fluxes in hot crucibles that have not been subjected to any postgrowth purification. The high value of *ℓ* in PdCoO₂ has important consequences for a number of physical properties, for example, the out-of-plane magnetoresistance, which is huge and strongly varies with field angle (19), behavior consistent with observation of the long-sought “axial anomaly” (20, 21).

The subject of this paper, PtCoO₂, offers an opportunity to extend the study of the intriguing metallic delafossite oxides to a 5d system where spin-orbit coupling (SOC) is considerably stronger. Although crystal growth (2) and room temperature resistivity (3) were reported over 40 years ago, no temperature-dependent transport studies were carried out on those crystals, and further crystal growth proved to be extremely challenging. Here, we describe crystal growth using a different method to those previously attempted in PtCoO₂. This yields high-quality single crystals large enough for spectroscopic measurements. From angle-resolved photoemission spectroscopy (ARPES), combined with density functional theory calculations and precise transport measurements performed on focused ion beam patterned crystals, we show that PtCoO₂ hosts ultrahigh conductivity derived from a single half-filled and nearly free-electron-like Pt 5*d* band.

RESULTS

Single crystals

First, we describe our crystal growth. Shannon (22) reported single crystal growth of Pt_{*x*}Co_{*y*}O₂ (where *x* and *y* were 0.85 ± 0.15) several decades ago. Stoichiometric PtCoO₂ was grown only under high pressure (3000 atm), with other growth conditions resulting only in

¹Max Planck Institute for Chemical Physics of Solids, Nöthnitzer Straße 40, 01187 Dresden, Germany. ²Scottish Universities Physics Alliance, School of Physics and Astronomy, University of St. Andrews, St. Andrews, Fife KY16 9SS, UK. ³Laboratory for Solid State Physics, ETH Zurich, CH-8093 Zurich, Switzerland. ⁴Diamond Light Source, Harwell Campus, Didcot, Oxfordshire OX11 0DE, UK.

*Corresponding author. E-mail: andy.mackenzie@cpfs.mpg.de (A.P.M.); philip.king@st-andrews.ac.uk (P.D.C.K.)

nonstoichiometric crystals. Tanaka *et al.* (23) were able to grow stoichiometric PtCoO₂ by using a metathetical reaction under vacuum, but the crystal size was limited to 30 μm. Here, we used a technique similar to that applied by Takatsu *et al.* (24) to the growth of PdCoO₂ (see Materials and Methods) to realize large stoichiometric PtCoO₂ single crystals.

Figure 1A shows optical pictures of the as-grown crystals. They form as triangular or hexagonal plates. Terrace-type lateral growth leads to variation in crystal thickness from one side to another as evident from Fig. 1A. However, there were many crystals with uniform thickness without any steps. Because of their brittleness and layered nature, the typical size of these crystals varies from in-plane dimensions of a few micrometers to 0.3 mm, with a maximum thickness of 3 μm. Bigger crystals were grown after using modified techniques with more complex temperature profiles (25). A cluster of such big as-grown crystals is shown in the inset of Fig. 1A. These crystals were used for the ARPES measurements discussed below. Single crystals were mechanically separated using a scalpel and then separated from unreacted CoO and from CoCl₂ powder by cleaning the product with boiling alcohol. All crystals were characterized by a scanning electron microscope (SEM) with an electron probe microanalyzer and confirmed to be single phase with no inclusions. Le Bail fitting of the powder x-ray diffraction (XRD) pattern was performed using space group $R\bar{3}m$ (space group no. 166). The experimental XRD pattern along with the fitted pattern and the difference between the two are shown in Fig. 1B. The refined lattice parameters are $a = 2.82259(\pm 5)$ Å and $c = 17.8084(\pm 3)$ Å.

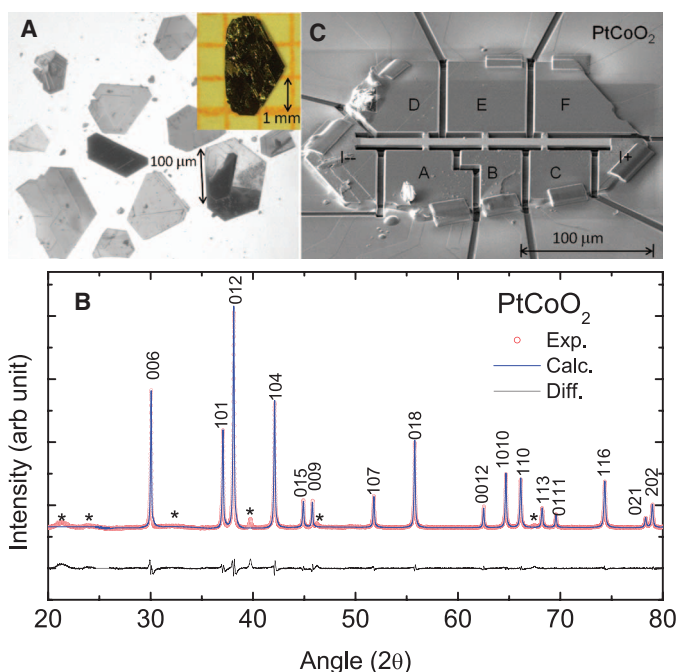


Fig. 1. Single-crystal PtCoO₂ samples. (A) Optical microscope image of as-grown crystals of PtCoO₂. (B) Le Bail fitting of powder XRD pattern along with the fitted and the difference curve. All peaks are labeled with corresponding hkl values. Peaks marked with "*" correspond to unavoidable unreacted PtCl₂ stuck to the crystal surface. (C) SEM image of a sample used for transport measurements in which a focused ion beam was used to define a measurement track of well-defined geometry.

Transport measurements

Because the resistivity of PtCoO₂ is very low (3), it was challenging to obtain accurate absolute values of resistivity because of uncertain geometrical factors. To overcome this, and to enhance the precision with which we could measure even smaller resistances at low temperatures, we made use of focused ion beam techniques to prepare samples with well-defined geometries (26). One example, along with its dimensions (length between two voltage contacts, 40 μm; width, is 8.4 μm; thickness, is 2.6 μm), is shown in Fig. 1C.

In Fig. 2, we show the in-plane resistivity of PtCoO₂ crystals from the growth run described above. In total, about 10 crystals were studied, and the reproducibility of the temperature dependence was excellent. The data are from the well-defined microstructure shown in Fig. 1, allowing the absolute value of resistivity to be determined with an accuracy of better than 5%. At room temperature, $\rho = 2.1$ microhm-cm, the lowest ever measured in an oxide metal. This is 20% lower than that of PdCoO₂ (18) and about a factor of 4 (27) and 12 (28) lower than in ReO₃ and IrO₂, respectively, which are themselves famous examples of good $5d$ oxide conductors. The resistivity decreases to less than 40 nanohm-cm at 16 K but then rises again by about 4% between 16 and 2 K, as shown in the inset of Fig. 2A. The residual resistivity ratio ρ_{300K}/ρ_{15K} is typically 50 to 60. The upturn is consistently observed in both as-grown crystals

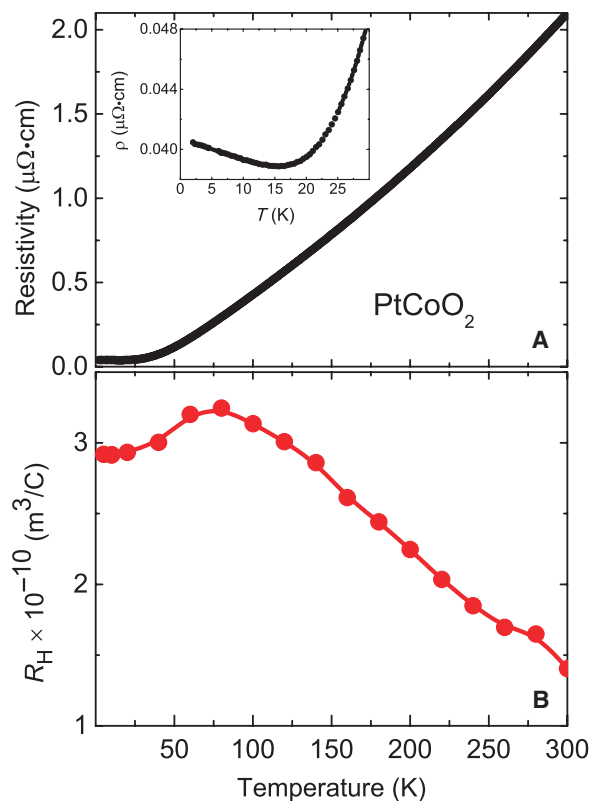


Fig. 2. Temperature-dependent transport. (A) The temperature-dependent in-plane resistivity of PtCoO₂ in zero applied magnetic field. The inset shows a magnified view of the low-temperature resistivity, revealing an upturn below 16 K. (B) Temperature dependence of the Hall coefficient (R_H), calculated by taking the field gradient between 7 and 9 T of the data shown in fig. S1.

and those that were microstructured with the focused ion beam, so we are certain that it is not the result of ion beam-induced disorder. The measured magnetoresistance of PtCoO₂ is positive for all temperatures above 2 K, making it unlikely that the Kondo effect is the cause of the upturn. Its origin will be the subject of further investigation.

In Fig. 2B, we show the measured Hall coefficient deduced from measurements of the transverse resistivity of the device shown in Fig. 1C (see also fig. S1). Below 20 K, the data are dominated by the high-field regime in which the Fermi surface volume alone is expected to determine the value of the Hall coefficient (29). The value in that region is about $2.9 \times 10^{-10} \text{ m}^3/\text{C}$, close to the value that we measure for PdCoO₂ under the same conditions, and within 10% of the expectation for a single band containing one electron per Pt.

Electronic structure

Our ARPES measurements (Fig. 3) directly reveal just such a Fermi surface, composed of a single electron pocket centered at the Γ point of the Brillouin zone. The sharp spectral features are indicative of quasi-two-dimensional electronic states (30). The near-hexagonal Fermi surface, rotated by 30° with respect to the Brillouin zone, is qualitatively similar to that of the bulk Fermi surface of PdCoO₂ (31). We find, however, that the PtCoO₂ Fermi surface has sharper corners and slightly concave faces. This is consistent with previous first-principles calculations (32), as well as our own density functional theory results (Fig. 3B). Our calculations predict an additional hole band in the vicinity of E_F at the zone edge (Fig. 4A), whose position delicately depends on the oxygen position (0,0,z) as shown in fig. S2B. Neglecting SOC, this intersects the Fermi level when using either the experimental (2) or fully relaxed oxygen positions, creating additional small lens-shaped Fermi surface pockets. Including SOC, however, lowers these bands by ~100 meV, pushing them below the Fermi level. Spin-orbit interactions therefore stabilize a robust single-band Fermi surface in PtCoO₂, consistent with our ARPES measurements as well as recent de Haas-van Alphen results (33).

The Fermi surface area we extract from ARPES, by fitting MDCs as a function of angle around the Brillouin zone, is $2.6 \pm 0.1 \text{ \AA}^{-2}$. The

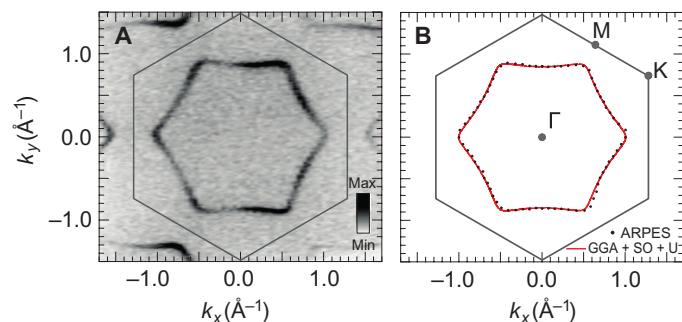


Fig. 3. Single-band faceted Fermi surface. (A) Fermi surface of PtCoO₂ measured by ARPES integrated over $E_F \pm 5 \text{ meV}$. The solid line represents the Brillouin zone. (B) The Fermi surface area is 8% smaller than would be expected for a half-filled band, as discussed in the main text, but its shape is in agreement with the Fermi surface obtained from GGA (general gradient approximation) + SO (spin orbit) + U calculations ($U = 4 \text{ eV}$), shown in red and scaled to match the experimental area. The dots represent the Fermi momenta extracted from (A) by radially fitting momentum distribution curves (MDCs) around the measured Fermi surface.

corresponding Luttinger count, assuming perfect two-dimensionality, is $n = (0.92 \pm 0.05)e^-$. This is comparable to ARPES measurements of PdCrO₂ (34) but is slightly smaller than that expected for a half-filled zone derived from a single conduction electron per Pt. In contrast, de Haas-van Alphen measurements indicate a Luttinger count within 2% of half-filling. We thus ascribe the deviations in our ARPES measurements as due to a possible small difference in surface chemistry from the bulk, sample-to-sample stoichiometry variations, or surface charge transfer. Nonetheless, we find almost perfect agreement of the shape of our measured Fermi surface with our calculations from density functional theory scaled to have the same area (Fig. 3B). We therefore conclude that our measurements are indicative of the bulk electronic structure of PtCoO₂. We note that, at lower photon energies, weak spectral features emerge, giving rise to shoulders on the states reported here and residual spectral weight at the zone center. In comparison to previous surface electronic structure calculations for PdCoO₂ (16) and ARPES measurements of PdCrO₂ (34), we attribute these to Pt-terminated

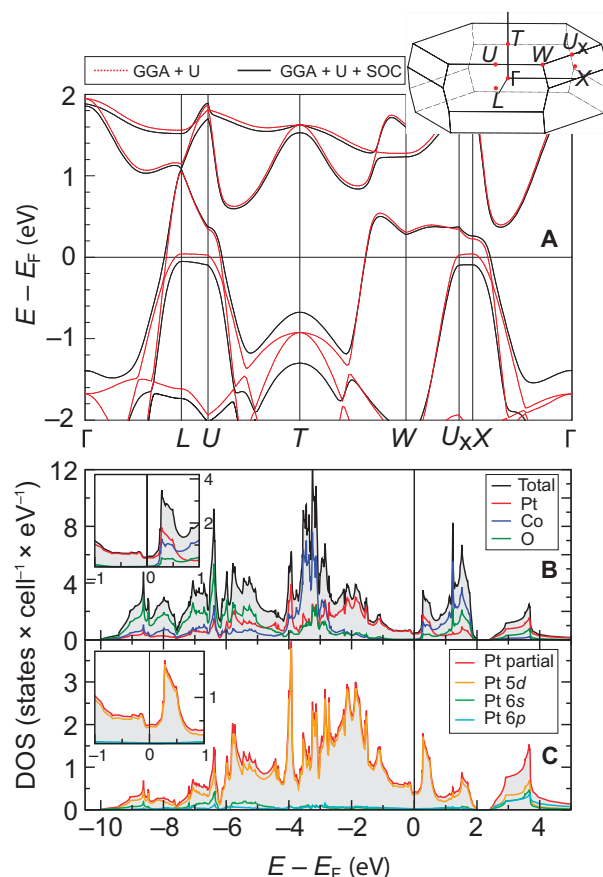


Fig. 4. Electronic structure. (A) Calculated bulk electronic structure (see Materials and Methods) with and without SOC. The high-symmetry points are labeled on the bulk Brillouin zone (inset). Inclusion of SOC pushes the hole bands at, for example, the L -point below E_F while leaving the remaining bands crossing the Fermi level almost unchanged. (B and C) Partial (B) and orbitally resolved (C) density of states (DOS) (including SOC), revealing the states at E_F to originate almost exclusively from Pt 5d.

surface states not visible at the higher photon energies shown here because of photoemission cross-section variations (35), although their weak weight precludes an unambiguous assignment between these features. Other cleaves showed stronger surface-derived features but a bulk band in quantitative agreement with the one found here.

Figure 5A shows the bulk band dispersion measured along the $\Gamma - K$ direction. Consistent with our measured Fermi surface, we find a single band in the vicinity of E_F . It is extremely steep, dispersing by less than 5% of the Brillouin zone over the energy range of 0.6 eV below the Fermi level shown in Fig. 5A. Indeed, from fits to MDCs, we find negligible deviations from linearity over a range exceeding 0.25 eV below E_F , together with a high Fermi velocity of $(8.9 \pm 0.5) \times 10^5$ m/s [5.8 ± 0.3 eV $\text{\AA}/\hbar$]. This is several times larger than observed in other metallic 5d oxides (36, 37) and yields an effective mass, $m^* = 1.09m_e$, within 10% of the free-electron mass. With no free parameters, using this effective mass within a simple parabolic model reproduces our measured dispersion over an extended energy range well (Fig. 5A).

The Fermi velocity [$(8.9 \pm 0.9) \times 10^5$ m/s] that we extract along $\Gamma - M$ is the same as that along $\Gamma - K$ within our experimental resolution (Fig. 5B). This is almost 20% higher than that measured along the $\Gamma - M$ direction in PdCoO₂ (31). Because of the higher k_F along $\Gamma - M$ than $\Gamma - K$, the effective mass obtained from our measured Fermi velocity, $m^* = 1.27m_e$, deviates further from the free-electron mass. The average mass of $m^* = 1.18m_e$ is in agreement with the value of $m^* = (1.14 \pm 0.05)m_e$ obtained from quantum oscillations of PtCoO₂ (33)

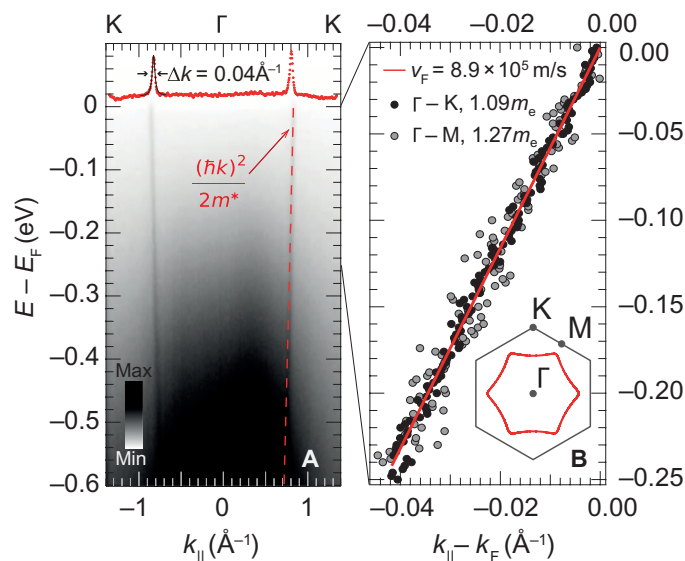


Fig. 5. Weakly interacting quasiparticle dispersion. (A) Electronic structure along the $\Gamma - K$ direction. The single band crossing the Fermi level can be traced down to more 0.5 eV binding energy with little broadening. The dashed red line corresponds to a parabolic dispersion with an effective mass $m^* = 1.09m_e$. An MDC at the Fermi level ($E_F \pm 6$ meV) is shown by the dots, with a fit to a Lorentzian peak indicating a full width at half maximum of 0.04 \AA^{-1} . (B) The gray and black dots represent the peak positions of the fits to the MDCs along the $\Gamma - M$ and $\Gamma - K$ direction, respectively. A linear fit to each data set independently yields a Fermi velocity of 8.9×10^5 m/s (shown by the solid line), giving an effective mass of $1.09m_e$ along $\Gamma - K$ and $1.27m_e$ along $\Gamma - M$.

and is again notably smaller than the values of about $1.5m_e$ obtained for PdCoO₂ (18).

DISCUSSION

The above measurements point to light quasiparticles in this system, in keeping with their extremely high conductivity, with an even wider electronic bandwidth of the state crossing E_F in PtCoO₂ than the Pd-derived sister compound. In PdCoO₂, it has proved controversial whether the high conductivity and low effective masses are mediated by significant Pd *s-d* orbital mixing (3, 14, 18, 31, 38). To specifically address this issue, we have performed our density functional calculations using a local-orbital rather than plane-wave basis (see Materials and Methods), which allows a well-justified assignment of orbital characters. We find that the density of states at the Fermi level predominantly originates from Pt states, with almost 90% Pt-related character. About 85% of these states belong to the Pt 5d orbitals with only a small admixture of Pt 6s and Pt 6p (Fig. 4B). Because of the localized nature of the Co 3d shell, the strong Coulomb repulsion for these states was explicitly taken into account (see fig. S2 and Materials and Methods). This suppresses an unphysical hybridization of the Co 3d states with the Pt 5d states near the Fermi level, which causes a pronounced rounding of alternating Fermi surface corners in contrast to the experiment. This suppression occurs for $U_{3d} \gtrsim 3$ eV, after which the Fermi surface topology and its orbital character are insensitive to the value of U_{3d} used over our investigated range of up to 6 eV. The Pt *d*-orbital-derived nature of the Fermi surface found here is entirely in keeping with its faceted nature, whereas the increase of electronic bandwidth compared to PdCoO₂ can naturally be understood from the spatially more extended nature of Pt 5d than Pd 4d orbitals. Remarkably, the effective masses we observe here are a factor of 2 to 3 smaller than even those of the strongly *s-d* hybridized electron Fermi surface sheets in Pt metal (39).

From the bulk Fermi surface, we can straightforwardly convert our resistivity measurements shown in Fig. 2 to a temperature-dependent mean free path, which we find rises from 700 \AA at room temperature to as high as 4 μm at 16 K. This is qualitatively consistent with the sharp spectral features we observe in ARPES. We observe narrow linewidths of MDCs at the Fermi level of better than 0.04 \AA^{-1} (Fig. 5A), very similar to those previously reported for PdCoO₂ (31) and comparable to our experimental angular resolution. These remain clearly resolved to high binding energies, with $\lesssim 0.01 \text{ \AA}^{-1}$ increase in linewidth over the first 350 meV binding energy range. This indicates a striking resilience of the quasiparticle lifetime away from the Fermi level, suggesting weak electron-electron scattering in PtCoO₂. This is in contrast to other well-known Fermi liquid oxide metals such as Sr₂RuO₄ (40) and Sr₂RhO₄ (41), which host sharp spectral features at low energy but rapidly develop substantial broadening away from E_F . Additionally, those systems host moderate correlation-induced enhancements of the effective mass. The lack of both of these features here points to a particularly weak influence of electron-electron interactions on the electronic structure of PtCoO₂.

This is not the situation in all quasi-two-dimensional 5d transition-metal oxides. In the layered iridates, for example, electronic correlations are still strong enough to drive a Mott-like transition to an insulating state once structural distortions and strong SOC collectively narrow the electronic bandwidth (37, 42, 43). In contrast, itineracy is preserved in

PtCoO₂ by the isolated single-band nature of the Fermi surface. In the absence of band-folding arising from structural distortions, not present in PtCoO₂, this band remains relatively unaffected by SOC, whereas large hybridization gaps are only opened away from E_F where band crossings between different orbital character states occur (see, for example, around the T point in Fig. 4A, where a $d_{xz/yz}$ degeneracy is lifted by about 600 meV). Thus, the bandwidth of the state crossing E_F in PtCoO₂ remains large, away from the narrow-band $J_{\text{eff}} = 1/2$ limit of the iridates. This naturally renders the electronic correlations expected of a $5d$ system insufficient to drive a Mott transition. Nonetheless, the extremely good metallicity and lack of spectral broadening away from E_F point not only to large bare bandwidths but also to suppressed electron-electron interactions compared to other wide-band transition-metal oxides. Indeed, the fact that the Fermi velocities shown in Fig. 5B are so close to the free-electron values is itself remarkable, because the highly faceted Fermi surface demonstrates the influence of the lattice potential on the states near E_F . Nonetheless, our measurements firmly establish PtCoO₂ as a model half-filled nearly free-electron oxide metal, with high-quality crystals rendering this system an ideal test bed for future studies of the nature of electronic correlations and the origins of extremely good metallicity in both Pt- and Pd-based delafossite oxides.

MATERIALS AND METHODS

Single crystal growth

Powders of reagent-grade PtCl₂ (99.99+% purity; Alfa Aesar) and CoO (99.995% purity; Alfa Aesar) were ground together for about an hour under an inert atmosphere in accordance with the chemical reaction $\text{PtCl}_2 + 2\text{CoO} \rightarrow \text{PtCoO}_2 + \text{CoCl}_2$. The mixed powder was then sealed in a quartz tube under a vacuum of 5×10^{-6} torr. The sealed quartz tube was heated in a vertical furnace to 800°C for 5 hours and cooled down to 740°C at a rate of 7.5°C/hour and kept at this temperature for 30 hours. Finally, the furnace was cooled from 740°C to room temperature at a rate of 90°C/hour.

Transport

Transport measurements were performed using standard four-probe ac techniques in ⁴He cryostats (Quantum Design), with measurement frequencies in the range of 50 to 200 Hz, magnetic fields of up to 14 T, and the use of single-axis rotators. The Hall effect was studied using reversed-field sweeps in the range of $-9 \text{ T} < B < 9 \text{ T}$ at a series of fixed temperatures.

Angle-resolved photoemission

ARPES measurements were performed using the I05 beamline of Diamond Light Source, UK. Samples were cleaved in situ at the measurement temperature of ~6 K. Measurements shown in Figs. 3 and 5 were performed using 110 and 118 eV p -polarized light, respectively. A Scienta R4000 hemispherical analyzer was used for all the measurements.

Density functional theory calculations

Relativistic density functional electronic structure calculations were performed using the full-potential FPLO code (44, 45) version fplo14.00-47. For the exchange-correlation potential, within the GGA, the parameterization of Perdew-Burke-Ernzerhof (46) was chosen. The SOC was nonperturbatively treated, solving the four-component Kohn-Sham-Dirac equation (47). To obtain precise band structure and Fermi surface

information, we carried out the calculations on a well-converged mesh of 27,000 k -points ($30 \times 30 \times 30$ mesh, 2496 points in the irreducible wedge of the Brillouin zone). The strong Coulomb repulsion in the Co $3d$ shell was taken into account in a mean field way applying the GGA + U approximation (48) in the atomic-limit (AL) flavor. For all calculations, the experimental lattice parameters have been used.

SUPPLEMENTARY MATERIALS

Supplementary material for this article is available at <http://advances.sciencemag.org/cgi/content/full/1/9/e1500692/DC1>

Hall effect measurement

Fig. S1. Field-dependent Hall effect measurements.

Calculated density of states

Fig. S2. Additional density-of-states calculations.

Reference (49)

REFERENCES AND NOTES

- R. D. Shannon, D. B. Rogers, C. T. Prewitt, Chemistry of noble metal oxides. I. Syntheses and properties of ABO₂ delafossite compounds. *Inorg. Chem.* **10**, 713–718 (1971).
- R. D. Shannon, C. T. Prewitt, D. B. Rogers, Chemistry of noble metal oxides. II. Crystal structures of PtCoO₂, PdCoO₂, CuFeO₂, and AgFeO₂. *Inorg. Chem.* **10**, 719–723 (1971).
- R. D. Shannon, D. B. Rogers, C. T. Prewitt, J. L. Gillson, Chemistry of noble metal oxides. III. Electrical transport properties and crystal chemistry of ABO₂ compounds with the delafossite structure. *Inorg. Chem.* **10**, 723–727 (1971).
- M. A. Marquardt, N. A. Ashmore, D. P. Cann, Crystal chemistry and electrical properties of the delafossite structure. *Thin Solid Films* **496**, 146–156 (2006).
- D. J. Singh, Electronic and thermoelectric properties of CuCoO₂: Density functional calculations. *Phys. Rev. B* **76**, 085110 (2007).
- F. Wang, A. Vishwanath, Spin phonon induced collinear order and magnetization plateaus in triangular and kagome antiferromagnets: Applications to CuFeO₂. *Phys. Rev. Lett.* **100**, 077201 (2008).
- H. Yanagi, T. Hase, S. Ibuki, K. Ueda, H. Hosono, Bipolarity in electrical conduction of transparent oxide semiconductor CuInO₂ with delafossite structure. *Appl. Phys. Lett.* **78**, 1583 (2001).
- H. Takatsu, H. Yoshizawa, S. Yonezawa, Y. Maeno, Critical behavior of the metallic triangular-lattice Heisenberg antiferromagnet PdCrO₂. *Phys. Rev. B* **79**, 104424 (2009).
- H. Takatsu, S. Yonezawa, S. Fujimoto, Y. Maeno, Unconventional anomalous hall effect in the metallic triangular-lattice magnet PdCrO₂. *Phys. Rev. Lett.* **105**, 137201 (2010).
- J. M. Ok, Y. J. Jo, K. Kim, T. Shishidou, E. S. Choi, H.-J. Noh, T. Oguchi, B. I. Min, J. S. Kim, Quantum oscillations of the metallic triangular-lattice antiferromagnet PdCrO₂. *Phys. Rev. Lett.* **111**, 176405 (2013).
- H. Takatsu, G. Nénert, H. Kadowaki, H. Yoshizawa, M. Enderle, S. Yonezawa, Y. Maeno, J. Kim, N. Tsuji, M. Takata, Y. Zhao, M. Green, C. Broholm, Magnetic structure of the conductive triangular-lattice antiferromagnet PdCrO₂. *Phys. Rev. B* **89**, 104408 (2014).
- C. W. Hicks, A. S. Gibbs, L. Zhao, P. Kushwaha, H. Borrmann, A. P. Mackenzie, H. Takatsu, S. Yonezawa, Y. Maeno, E. A. Yelland, Quantum oscillations and magnetic reconstruction in the delafossite PdCrO₂. *Phys. Rev. B* **92**, 014425 (2015).
- A. I. Coldea, L. Seabra, A. McCollam, A. Carrington, L. Malone, A. F. Bangura, D. Vignolles, P. G. van Rhee, R. D. McDonald, T. Sörgel, M. Jansen, N. Shannon, R. Coldea, Cascade of field-induced magnetic transitions in a frustrated antiferromagnetic metal. *Phys. Rev. B* **90**, 020401(R) (2014).
- V. Eyert, R. Frésard, A. Maignan, On the metallic conductivity of the delafossites PdCoO₂ and PtCoO₂. *Chem. Mater.* **20**, 2370–2373 (2008).
- R. Seshadri, C. Felser, K. Thieme, W. Tremel, Metal-metal bonding and metallic behavior in some ABO₂ delafossites. *Chem. Mater.* **10**, 2189–2196 (1998).
- K. Kim, H. C. Choi, B. I. Min, Fermi surface and surface electronic structure of delafossite PdCoO₂. *Phys. Rev. B* **80**, 035116 (2009).
- H.-J. Noh, J. Jeong, J. Jeong, H. Sung, K. J. Park, J.-Y. Kim, H.-D. Kim, S. B. Kim, K. Kim, B. I. Min, Orbital character of the conduction band of delafossite PdCoO₂ studied by polarization-dependent soft x-ray absorption spectroscopy. *Phys. Rev. B* **80**, 073104 (2009).
- C. W. Hicks, A. S. Gibbs, A. P. Mackenzie, H. Takatsu, Y. Maeno and E. A. Yelland, Quantum oscillations and high carrier mobility in the delafossite PdCoO₂. *Phys. Rev. Lett.* **109**, 116401 (2012).

19. H. Takatsu, J. J. Ishikawa, S. Yonezawa, H. Yoshino, T. Shishidou, T. Oguchi, K. Murata, Y. Maeno, Extremely large magnetoresistance in the nonmagnetic metal PdCoO₂. *Phys. Rev. Lett.* **111**, 056601 (2013).
20. N. Kikugawa, P. Goswami, A. Kiswandhi, E. S. Choi, D. Graf, R. E. Baumbach, J. S. Brooks, K. Sugii, Y. Iida, M. Nishio, S. Uji, T. Terashima, P. M. C. Rourke, N. E. Hussey, H. Takatsu, S. Yonezawa, Y. Maeno, L. Balicas, Realization of the axial anomaly in a quasi-two-dimensional metal. arXiv:1412.5168
21. P. Goswami, J. H. Pixley, S. D. Sarma, Axial anomaly and longitudinal magnetoresistance of a generic three dimensional metal. *Phys. Rev. B* **92**, 075205 (2015).
22. R. D. Shannon, Electrically conductive platinum cobalt oxides. U.S. Patent 3,514,414 (1970).
23. M. Tanaka, M. Hasegawa, H. Takei, Crystal growth of PdCoO₂, PtCoO₂ and their solid-solution with delafossite structure. *J. Cryst. Growth* **173**, 440–445 (1997).
24. H. Takatsu, S. Yonezawa, S. Mouri, S. Nakatsujii, K. Tanaka, Y. Maeno, Roles of high-frequency optical phonons in the physical properties of the conductive delafossite PdCoO₂. *J. Phys. Soc. Jpn.* **76**, 104701 (2007).
25. P. Kushwaha, C. Geibel, M. P. Schmidt, A. P. Mackenzie *et al.*, to be published.
26. P. J. W. Moll, R. Puzniak, F. Balakirev, K. Rogacki, J. Karpinski, N. D. Zhigadlo, B. Batlogg, High magnetic-field scales and critical currents in SmFeAs(O, F) crystals. *Nat. Mater.* **9**, 628–633 (2010).
27. T. P. Pearsall, C. A. Lee, Electronic transport in ReO₃: dc conductivity and Hall effect. *Phys. Rev. B* **10**, 2190 (1974).
28. W. D. Ryden, A. W. Lawson, C. C. Sartain, Temperature dependence of the resistivity of RuO₂ and IrO₂. *Phys. Lett. A* **26**, 209–210 (1968).
29. C. M. Hurd, *The Hall Effect in Metals and Alloys* (Springer, Boston, MA, 1972).
30. J. M. Riley, F. Mazzola, M. Dendzik, M. Michiardi, T. Takayama, L. Bawden, C. Granerød, M. Leandersson, T. Balasubramanian, M. Hoesch, T. K. Kim, H. Takagi, W. Meevasana, Ph. Hofmann, M. S. Bahrany, J. W. Wells, P. D. C. King, Direct observation of spin-polarized bulk bands in an inversion-symmetric semiconductor. *Nat. Phys.* **10**, 835–839 (2014).
31. H.-J. Noh, J. Jeong, J. Jeong, E.-J. Cho, S. B. Kim, K. Kim, B. I. Min, H.-D. Kim, Anisotropic electric conductivity of delafossite PdCoO₂ studied by angle-resolved photoemission spectroscopy. *Phys. Rev. Lett.* **102**, 256404 (2009).
32. K. P. Ong, D. J. Singh, P. Wu, Unusual transport and strongly anisotropic thermopower in PtCoO₂ and PdCoO₂. *Phys. Rev. Lett.* **104**, 176601 (2010).
33. F. Arnold, E. Hassinger *et al.*, to be published.
34. J. A. Sobota, K. Kim, H. Takatsu, M. Hashimoto, S.-K. Mo, Z. Hussain, T. Oguchi, T. Shishidou, Y. Maeno, B. I. Min, Z.-X. Shen, Electronic structure of the metallic antiferromagnet PdCrO₂ measured by angle-resolved photoemission spectroscopy. *Phys. Rev. B* **88**, 125109 (2013).
35. H.-J. Noh, J. Jeong, B. Chang, D. Jeong, H. S. Moon, E.-J. Cho, J. M. Ok, J. S. Kim, K. Kim, B. I. Min, H.-K. Lee, J.-Y. Kim, B.-G. Park, H.-D. Kim, S. Lee, Direct observation of localized spin antiferromagnetic transition in PdCrO₂ by angle-resolved photoemission spectroscopy. *Sci. Rep.* **4**, 3680 (2014).
36. A. de la Torre, E. C. Hunter, A. Subedi, S. McKeown Walker, A. Tamai, T. K. Kim, M. Hoesch, R. S. Perry, A. Georges, F. Baumberger, Coherent quasiparticles with a small Fermi surface in lightly doped Sr₃Ir₂O₇. *Phys. Rev. Lett.* **113**, 256402 (2014).
37. Y. F. Nie, P. D. C. King, C. H. Kim, M. Uchida, H. I. Wei, B. D. Faeth, J. P. Ruff, J. P. C. Ruff, L. Xie, X. Pan, C. J. Fennie, D. G. Schlom, K. M. Shen, Interplay of spin-orbit interactions, dimensionality, and octahedral rotations in semimetallic SrIrO₃. *Phys. Rev. Lett.* **114**, 016401 (2015).
38. M. Tanaka, M. Hasegawa, T. Higuchi, T. Tsukamoto, Y. Tezuka, S. Shin, H. Takei, Origin of the metallic conductivity in PdCoO₂ with delafossite structure. *Phys. B Condens. Matter* **245**, 157–163 (1998).
39. J. B. Ketterson, L. R. Windmiller, de Haas-van Alphen effect in platinum. *Phys. Rev. B* **2**, 4813 (1970).
40. A. Damascelli, D. H. Lu, K. M. Shen, N. P. Armitage, F. Ronning, D. L. Feng, C. Kim, Z.-X. Shen, T. Kimura, Y. Tokura, Z. Q. Mao, Y. Maeno, Fermi surface, surface states, and surface reconstruction in Sr₂RuO₄. *Phys. Rev. Lett.* **85**, 5194–5197 (2000).
41. F. Baumberger, N. J. C. Ingle, W. Meevasana, K. M. Shen, D. H. Lu, R. S. Perry, A. P. Mackenzie, Z. Hussain, D. J. Singh, Z.-X. Shen, Fermi surface and quasiparticle excitations of Sr₂RhO₄. *Phys. Rev. Lett.* **96**, 246402 (2006).
42. B. J. Kim, H. Jin, S. J. Moon, J.-Y. Kim, B.-G. Park, C. S. Leem, J. Yu, T. W. Noh, C. Kim, S.-J. Oh, J.-H. Park, V. Durairaj, G. Cao, E. Rotenberg, Novel $J_{\text{eff}} = 1/2$ Mott state induced by relativistic spin-orbit coupling in Sr₂IrO₄. *Phys. Rev. Lett.* **101**, 076402 (2008).
43. P. D. C. King, T. Takayama, A. Tamai, E. Rozbicki, S. McKeown Walker, M. Shi, L. Patthey, R. G. Moore, D. Lu, K. M. Shen, H. Takagi, F. Baumberger, Spectroscopic indications of polaronic behavior of the strong spin-orbit insulator Sr₃Ir₂O₇. *Phys. Rev. B* **87**, 241106(R) (2013).
44. K. Koepf, H. Eschrig, Full-potential nonorthogonal local-orbital minimum-basis band-structure scheme. *Phys. Rev. B* **59**, 1743 (1999).
45. I. Opahle, K. Koepf, H. Eschrig, Full-potential band-structure calculation of iron pyrite. *Phys. Rev. B* **60**, 14035 (1999).
46. J. P. Perdew, K. Burke, M. Ernzerhof, Generalized gradient approximation made simple. *Phys. Rev. Lett.* **77**, 3865–3868 (1996).
47. H. Eschrig, M. Richter, I. Opahle, Relativistic solid state calculations, in *Relativistic Electronic Structure Theory (Part II, Applications)*, P. Schwerdtfeger, Ed. (Elsevier, Amsterdam, 2004), pp. 723–776.
48. H. Eschrig, K. Koepf, I. Chaplygin, Density functional application to strongly correlated electron systems. *J. Solid State Chem.*, **176**, 482–495 (2003).
49. N. P. Ong, Geometric interpretation of the weak-field Hall conductivity in two-dimensional metals with arbitrary Fermi surface. *Phys. Rev. B Condens. Matter* **43**, 193–201 (1991).

Acknowledgments: We thank the Scientific Center for Optical and Electron Microscopy and P. Gasser of the ETH Zurich for supporting the focused ion beam work. We thank the Diamond Light Source for the access to beamline I05 that contributed to the results presented here. **Funding:** This work was supported by the Engineering and Physical Sciences Research Council, UK (grant EP/I031014/1). P.D.C.K. acknowledges support from the Royal Society through a University Research Fellowship. **Author contributions:** P.K. and M.P.S. performed the crystal growth; V.S., P.K., P.J.W.M., L.B., J.M.R., N.N., F.A., E.H., and P.D.C.K. performed the experimental measurements; H.R. performed the theoretical calculations; T.K.K. and M.H. built and maintained the ARPES end station and provided experimental support; and A.P.M. and P.D.C.K. were responsible for overall project planning and direction and wrote the paper with input and discussion from all co-authors. **Competing interests:** The authors declare that they have no competing interests. **Data and materials availability:** Data underpinning this publication can be accessed at <http://dx.doi.org/10.17630/7a88d794-d747-4aa2-a099-9335c5b702ec>.

Submitted 28 May 2015
Accepted 20 August 2015
Published 23 October 2015
10.1126/sciadv.1500692

Citation: P. Kushwaha, V. Sunko, P. J. W. Moll, L. Bawden, J. M. Riley, N. Nandi, H. Rosner, M. P. Schmidt, F. Arnold, E. Hassinger, T. K. Kim, M. Hoesch, A. P. Mackenzie, P. D. C. King, Nearly free electrons in a 5d delafossite oxide metal. *Sci. Adv.* **1**, e1500692 (2015).

This article is published under a Creative Commons license. The specific license under which this article is published is noted on the first page.

For articles published under [CC BY](#) licenses, you may freely distribute, adapt, or reuse the article, including for commercial purposes, provided you give proper attribution.

For articles published under [CC BY-NC](#) licenses, you may distribute, adapt, or reuse the article for non-commercial purposes. Commercial use requires prior permission from the American Association for the Advancement of Science (AAAS). You may request permission by clicking [here](#).

The following resources related to this article are available online at <http://advances.sciencemag.org>. (This information is current as of October 26, 2015):

Updated information and services, including high-resolution figures, can be found in the online version of this article at:

<http://advances.sciencemag.org/content/1/9/e1500692.full.html>

Supporting Online Material can be found at:

<http://advances.sciencemag.org/content/suppl/2015/10/20/1.9.e1500692.DC1.html>

This article **cites 43 articles**, 0 of which you can be accessed free:

<http://advances.sciencemag.org/content/1/9/e1500692#BIBL>

Science Advances (ISSN 2375-2548) publishes new articles weekly. The journal is published by the American Association for the Advancement of Science (AAAS), 1200 New York Avenue NW, Washington, DC 20005. Copyright is held by the Authors unless stated otherwise. AAAS is the exclusive licensee. The title *Science Advances* is a registered trademark of AAAS